3-8-2011

Two rotary motors in F-ATP synthase are elastically coupled by a flexible rotor and a stiff stator stalk.

André Wächter

Yumin Bi

Stanley D Dunn

Brian D Cain

Hendrik Sielaff

See next page for additional authors

Authors
André Wächter, Yumin Bi, Stanley D Dunn, Brian D Cain, Hendrik Sielaff, Frank Wintermann, Siegfried Engelbrecht, and Wolfgang Junge

Two rotary motors in F-ATP synthase are elastically coupled by a flexible rotor and a stiff stator stalk

André Wächter[a,b], Yumin Bi[c], Stanley D. Dunn[c], Brian D. Cain[d], Hendrik Sielaff[a], Frank Wintermann[b], Siegfried Engelbrecht[b], and Wolfgang Junge[a,1]

Departments of [a]Biophysics and [b]Biochemistry, University of Osnabrück, 49069 Osnabrück, Germany; [c]Department of Biochemistry, University of Western Ontario, London, ON, Canada N6A 5C1; and [d]Department of Biochemistry and Molecular Biology, University of Florida, Gainesville, FL 32605

Edited* by John E. Walker, Medical Research Council Mitochondrial Biology Unit, Cambridge, United Kingdom, and approved January 21, 2011 (received for review August 5, 2010)

ATP is synthesized by ATP synthase (F_OF_1-ATPase). Its rotary electromotor (F_O) translocates protons (in some organisms sodium cations) and generates torque to drive the rotary chemical generator (F_1). Elastic power transmission between F_O and F_1 is essential for smoothing the cooperation of these stepping motors, thereby increasing their kinetic efficiency. A particularly compliant elastic domain is located on the central rotor ($c_{10–15}/\epsilon/\gamma$), right between the two sites of torque generation and consumption. The hinge on the active lever on subunit β adds further compliance. It is under contention whether or not the peripheral stalk (and the "stator" as a whole) also serves as elastic buffer. In the enzyme from *Escherichia coli*, the most extended component of the stalk is the homodimer b_2, a right-handed α-helical coiled coil. By fluctuation analysis we determined the spring constant of the stator in response to twisting and bending, and compared wild-type with b-mutant enzymes. In both deformation modes, the stator was very stiff in the wild type. It was more compliant if b was elongated by 11 amino acid residues. Substitution of three consecutive residues in b by glycine, expected to destabilize its α-helical structure, further reduced the stiffness against bending deformation. In any case, the stator was at least 10-fold stiffer than the rotor, and the enzyme retained its proton-coupled activity.

ATP synthesis | bioenergetics | nanomotor | protein elasticity

ATP synthase (F_OF_1-ATPase) produces ATP, the universal fuel of the cell, from ADP and orthophosphate (P_i). F_OF_1 is powered by the electrochemical potential difference of protons, in some organisms of sodium cations, across the respective coupling membrane (see refs. 1 and 2 for recent reviews). Fig. 1*A* illustrates the structure of *Escherichia coli* F_OF_1 (EF_OF_1) and the nomenclature of its eight different subunits. The central rotor (subunits $\gamma\epsilon\mathbf{c_{10}}$) is depicted in red and yellow, the catalytic hexagon $[(\alpha\beta)_3]$ in green and blue, and the peripheral stalk ($\delta\mathbf{b_2a}$) in gray. The stator's most extended portion is the homodimer $\mathbf{b_2}$ (3). This dimer is an unusual two-stranded right-handed coiled coil with the helices offset, rather than in-register (4, 5). Proton flow across the membrane-embedded, electrical nanomotor (F_O) generates torque, which is transmitted by the central shaft to the chemical reactor (F_1) that synthesizes ATP. The role of motor vs. generator can be reversed between F_O and F_1. Both are steppers, and their symmetries [always C_3 in F_1 (6) and $C_{10–15}$ in F_O depending on the organism (7)] may or may not match. The cooperation of the two stepping motors is smoothed by elastic power transmission (8–11) rather than by fine tuning of the respective partial reactions (12). This property accounts for (*i*) the high kinetic efficiency of F_OF_1, (*ii*) operation by the same principle with different gear ratios (3:10–15), and (*iii*) robust function of structurally modified enzyme constructs (10).

A search for the major elastic buffer between F_O and F_1 has been carried out with single molecules of EF_1 and EF_OF_1. Certain domains were stiffened by an engineered disulfide bridge, and the elastic stiffness of other domains was determined by recording their thermally agitated fluctuations (see ref. 13). The lower portion of the rotor, i.e., the contact region between subunits γ and ϵ with the $\mathbf{c_{10}}$ ring, has been identified as a particularly compliant domain. Located on the central rotor, right between the respective sites of torque generation in F_1 and F_O, and with a small torsional stiffness of only 70 pNnm or less (see below), it stores at least 14 kJ/mol elastic energy to smooth the cooperation of the two stepping motors when they work against each other. In the freely operating enzyme (no engineered disulfide bridges present) the hinge motion of the functional lever on the β-subunit adds to this compliance such that the total torsional stiffness is even lower (about 35 pNnm) (13). Preliminary experiments along the same lines have suggested that the stator of EF_OF_1 is very stiff. In contrast, it was previously suggested that the structure was inherently flexible, because neither the deletion of up to 11 nor the insertion of up to 14 amino acid residues in **b** fully deactivated EF_OF_1 (14, 15). Structural studies on the differently composed and differently shaped stator of the mitochondrial enzyme, on the other hand, have been interpreted to suggest its stiff rather than flexible construction (16–18). These diverging views have prompted us to directly assess the magnitude and the determinants of the elastic stiffness of the *E. coli* stator, comparing wild-type and mutant enzymes where **b** was either elongated by 11 amino acid residues or destabilized by substituting three consecutive residues with glycine.

Results

Forced Magneto-Rotation of the Stator with Attached Bead Identified Relevant Bead-Enzyme Constructs. Fig. 1 *B* and *C* illustrate the immobilization of EF_OF_1 and the attachment of a hyperparamagnetic bead to the stator. The bead was fluorescence labeled with Q dots. Their rotary motion was monitored in a fluorescence microscope and videographed at 25 frames per second. The rotation was either driven by an externally applied magnetic field or, in the absence of such a field, by thermal fluctuations. The detergent solubilized enzyme was fixed on a Ni-nitrilotriacetate (Ni-NTA) covered glass slide via engineered His tags on F_1, as previously noted (19). The Q-dot doped magnetic bead was attached to the enzyme via biotin-steptavidin or strep-tag-streptactin linkage in either of two modes. If the magnetic bead was attached to the N-terminal end of both copies of **b** (as illustrated in Fig. 1*B*) a rotating magnetic field twisted $\mathbf{b_2}$ around its long axis (see black double arrow in Fig. 1*B*). Alternatively, if the bead was attached to the $\mathbf{c_{10}}$ ring proper, and if the **a** subunit was locked to the $\mathbf{c_{10}}$ ring by a disulfide bridge (red bar in Fig. 1*C*), rotation around the long axis of the $\mathbf{c_{10}}$ ring (see red double ar-

Author contributions: S.D.D. and W.J. designed research; A.W. and Y.B. performed research; Y.B., S.D.D., B.D.C., F.W., and S.E. contributed new reagents/analytic tools; A.W., S.D.D., H.S., and W.J. analyzed data; and S.D.D. and W.J. wrote the paper.

The authors declare no conflict of interest.

*This Direct Submission article had a prearranged editor.

[1]To whom correspondence should be addressed. E-mail: junge@uos.de.

This article contains supporting information online at www.pnas.org/lookup/suppl/doi:10.1073/pnas.1011581108/-/DCSupplemental.

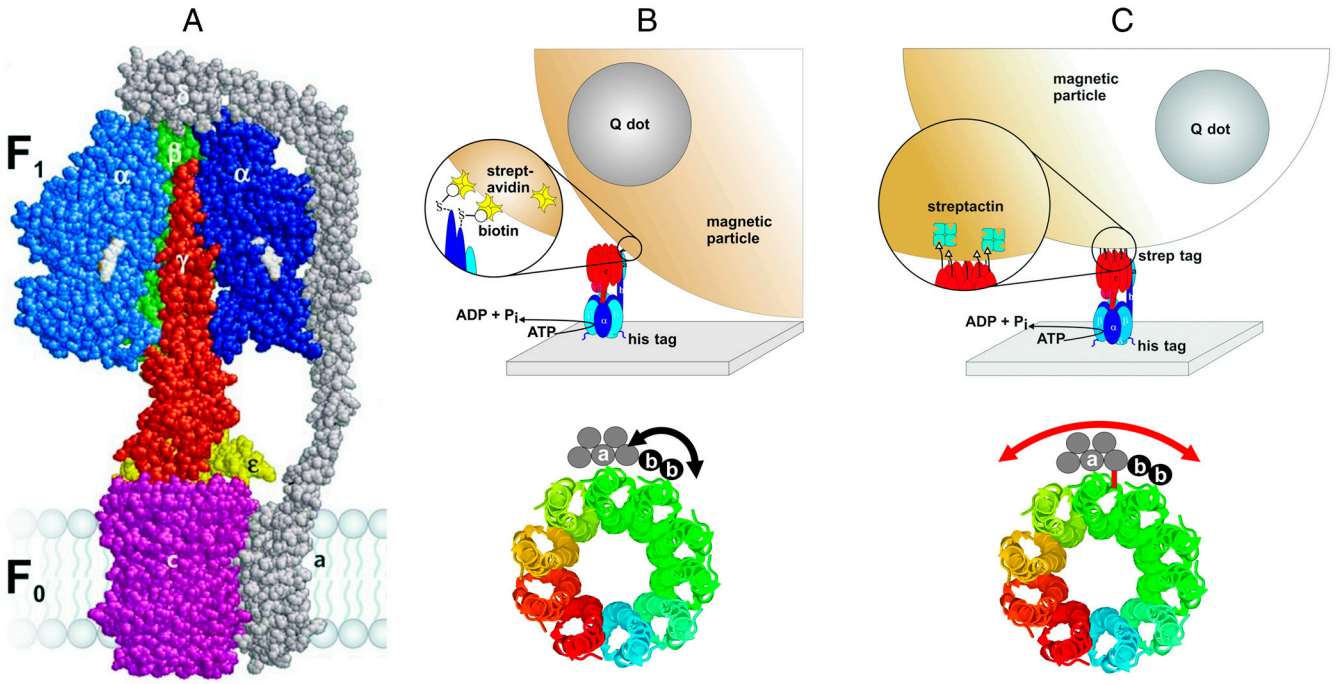

Fig. 1. (*A*) Space-filling homology model of EF_OF_1 (see legend for figure 1 in reference 1 for details) with one α-subunit and two β-subunits removed to expose the γ-subunit (red) in the center of the $(\alpha\beta)_3$-pseudohexagon, with α shown in blue, β in green, γ in red, ϵ in yellow, δ (on top) and subunits **a** and **b** in dark gray, nucleotides in pale gray, and $\mathbf{c}_{10}$ in magenta. The bulge of subunit γ (made up of the convex coiled coil consisting of the N- and C-terminal helices of γ) is not visible because it points away from the viewer. (*B* and *C*, *Upper*) The rotational assay for twisting (*B*) and bending (*C*) of $\mathbf{b}_2$ in immobilized and detergent-solubilized EF_OF_1. In *B*, the magnetic bead was attached directly to $\mathbf{b}_2$ via biotin-streptavidin. Magnetically forced rotation of the bead twisted $\mathbf{b}_2$ around its long axis. In *C*, the bead was attached via strep-tag-streptactin to the **c** ring. The **c** ring was locked to subunit **a** by an engineered disulfide bridge (see red bar in Fig. 1*C*). Magnetically forced rotation of the bead, and of the **c** ring around its central axis, bent $\mathbf{b}_2$ rather than twisting it as in *B*. The double arrows indicate the former and the latter deformation of the stator in black and red.

row) flexed $\mathbf{b}_2$ rather than twisting it as in Fig. 1*A*. The latter deformation of the stator resembles the physiological one when the two motors—EF_O generating torque by mediating proton flow and EF_1 generating countertorque by ATP hydrolysis—operate against each other. In both modes of attachment, limited rotary freedom was expected because the bead was attached to the stator that was, in turn, fixed to the solid support.

Two magnets were mounted at opposite positions on a rotating disk (0.107 revolutions per second) that was placed on top of the cover slide. Beads that followed the continuously rotating disk all around the clock were ignored. It was assumed that they were either wrongly attached to the enzyme (e.g., by one single bond only) or nonspecifically sticking to the solid support. Beads following the magnetic field only over a limited range were further evaluated. Broadly speaking, they followed the rotating field for up to +40°, remained there until the rotating disk had covered a quarter turn, and then snapped over into a position at −40°. The series of video frames in Fig. 2 shows the diffraction limited image of a fluorescent bead on a given single molecule of EF_OF_1 and, schematically, the position of the two magnets. The position of the two magnets relative to the relaxed bead-position (magnetic field off) was estimated (see the trajectories in Fig. S1 and Movie S1). The solid points and lines in the lower panels of Fig. 3 give the respective histograms of the bead orientation when the magnetic field was rotating either counterclockwise (red) or clockwise (blue).

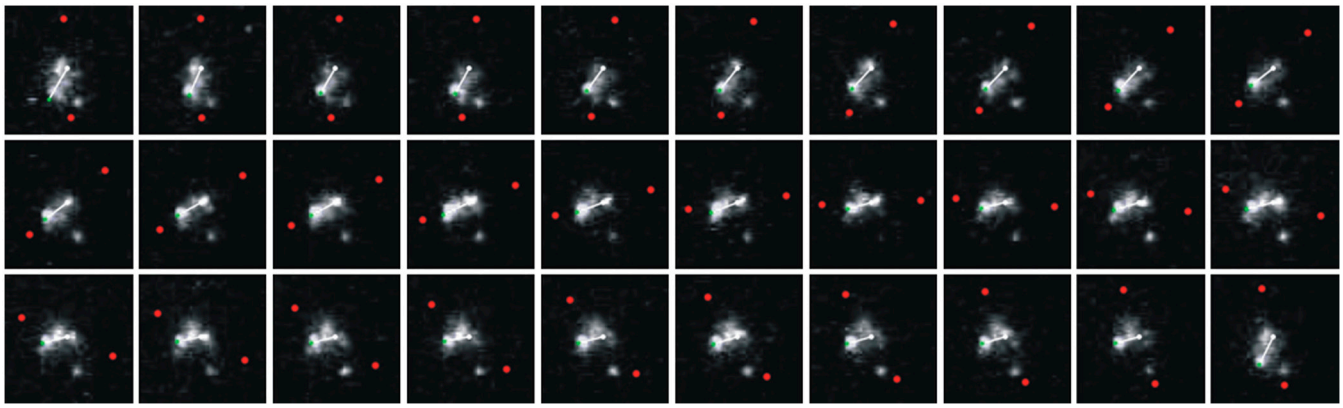

Fig. 2. Diffraction limited images of a fluorescent bead on a given single molecule of EF_OF_1 and, schematically, the position of the two magnets (in red) that were mounted on a rotating disk on top of the bead-enzyme construct (0.107 rev/s) [see the trajectory (Fig. S1) and Movie S1]. The radius of rotation is indicated by a white line reaching from the center to the farthermost end of the bead (in green). Every fourth frame of Movie S1 is shown.

Thermal Rotary Fluctuations of the Bead in the Absence of a Magnetic Field Yield the Elastic Stiffness of the Stator. The open data points in Fig. 3*A* were obtained by sampling rotary fluctuations over 3 min with the magnetic field switched off. The dashed curves in Fig. 3 *A–C* represent the respective fits by a single Gaussian, in red after previous clockwise, and in blue after previous counterclockwise rotation with the field on (solid curves). The Gaussian shape of fluctuations is typical of thermally activated rotation in a parabolic potential well. The torsional stiffness, κ^{rot}, is reciprocal to the variance, σ, according to Eq. **1** (see equation 4 in ref. 13):

$$\kappa^{\mathrm{rot}} = k_{\mathrm{B}}T \cdot \sigma^{-2}, \qquad [1]$$

wherein k_{B} denotes the Boltzmann constant, and T the temperature in Kelvin. If the FWHM of rotary fluctuations is taken in degrees, the stiffness in units of piconewton nanometer comes out as follows:$\kappa^{\mathrm{rot}} \approx 73700 \cdot (\mathrm{FWHM})^{-2}$. The FWHM in the two dashed curves in Fig. 3*A* was about 8°, implying a rotational stiffness of 1,150 pN nm.

Because the diameter of the beads is two orders of magnitude larger than the length of the enzyme, obstructive bead-surface contacts might have obscured the elastic properties of the enzyme. The following two criteria were taken as evidence that the enzyme, and not the surface, dominated the behavior: (*i*) symmetric peak structure in response to the clockwise and counterclockwise rotating field, and (*ii*) thermal fluctuations well centered to the former. Only symmetric datasets were further evaluated. Fig. 3 shows data from three different single molecules matching this condition. Fig. S2 shows asymmetric data that have been discarded.

Although the data with the rotating magnetic field on are of interest for nanoscopic magnetometry, nonlinearities, and hysteresis of the bead-enzyme construct, we refrained from an analysis because three properties were ill defined, namely, (*i*) the magnitude and direction of the magnetic field at the position of the bead, (*ii*) the anisotropy and linearity of the hyperparamagnetic beads, and (*iii*) the angular dependence of the magnetic field (see ref. 20 for such complications in electrorotation experiments on the flagellar motor).

The width of fluctuations is accurately recorded only under two conditions. (*i*) The sampling and averaging interval is long enough to yield a steady width, which holds true for intervals larger than 2 min (see Fig. S3). (*ii*) The video sampling frequency (here 25 s^{-1}) exceeds the "corner frequency" of the power spectrum of the overdamped motion (which has been discussed in the recent work by Noji and coworkers on TF_1; ref. 21). The latter condition was not always met in the present experiments. Averaging over high-frequency fluctuations during the video-frame duration of 40 ms narrowed the observed width and led to overestimation of the stiffness. The procedure of error correction (detailed in the *SI Text*) relates the apparent stiffness (κ_{app}) to the true one (κ) as follows,

$$\kappa = \frac{\arctan \omega_l/\omega_0}{\pi/2} \cdot \kappa_{\mathrm{app}} \qquad [2]$$

Herein ω_l denotes the cutoff frequency of the recorder, and ω_0 denotes the corner frequency of the Lorentzian power spectrum of the overdamped bead-enzyme construct (see ref. 22 and the respective paragraph in *SI Text*). It is noteworthy that the qualitative identification of stiff and compliant enzyme domains can be based on the apparent stiffness, even before correction, because it is monotonously related to the true stiffness (see *SI Text*).

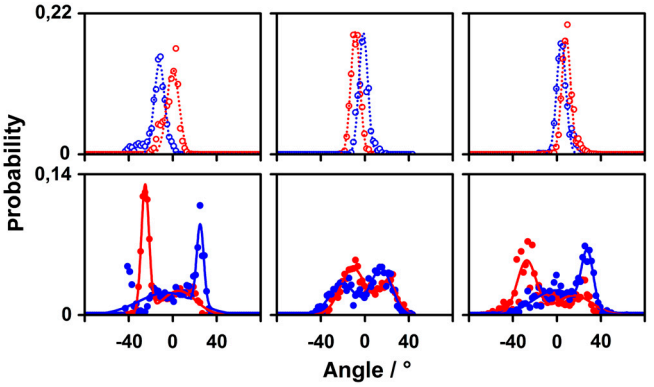

Fig. 3. Histograms of the bead orientation in the presence of a constantly rotating magnetic field (solid circles and curves) and in its absence, i.e., only under thermal agitation (open circles and dashed lines). The rotation rate was 0.107 rev/s, and the total observation time 3 min. Circles are experimental and lines represent a Gaussian fit. Solid lines, magnetically forced rotation in clockwise (red) and counterclockwise (blue) direction. Broken lines, thermally activated fluctuations (no magnetic field) after previous counterclockwise (blue) and clockwise (red) forced rotation, respectively. The histogram in each column was recorded with one and the same single molecule, and averaged over 3 min observation time. (*Left*) Mutant SD466 (3-gly); (*Center* and *Right*) SD460 (long).

Elastic Compliance of the Stator in Wild-Type and *b*-Mutant Enzymes. The rotary stiffness of the stator was determined in the wild type and in two mutants of subunit **b**, using either mode of bead attachment and stator deformation, namely, twisting (see Fig. 1*B*) and bending (see Fig. 1*C*). The sequences of these mutants are aligned in Fig. 4. The trivial names indicate the insertion of 11 residues ("long"), the substitution of three consecutive residues by glycine ("3-gly"), and the pseudo-wild-type, unmodified, and cysteine-free from residue Leu-3 to the C terminus ("wt*"). In the respective upper line, **b** carries a cysteine substitution at the second residue for the direct attachment of the bead (the twisting mode), and in the lower one it does not, and the bead is attached to the $\mathbf{c_{10}}$ ring, which is in turn cross-linked to **a** by an engineered disulfide bridge (the bending mode). Fig. S4 illustrates by red dots the C_α atoms of the three glycine substitutions in the slightly offset, right-handed coiled-coil model of $\mathbf{b_2}$ (5). This unusual coiled coil, originally postulated on the basis of biochemical and bioinformatic evidence (5), has found support from recent crystallographic analysis of the related heterodimeric complex from the *Thermus thermophilus* ATP synthase (23). The structural equivalent in the mitochondrial enzyme comprises more subunits (**b**, F_6, **d**) in a different arrangement (see ref. 16).

The apparent FWHM of thermal fluctuations of wt* and mutants under either mode of deformation are illustrated in Fig. 5. The black data in Fig. 5 were obtained for a bead attachment as shown in Fig. 1*B* where the coiled coil of $\mathbf{b_2}$ was twisted around its own long axis. Differences between the fluctuation widths of various mutants were small. The FWHM was centered around 7°, equivalent to an apparent stiffness of $\kappa^{\mathrm{twist}}_{\mathrm{app}}(\mathrm{stator}) = 1{,}500$ pNnm. This figure, after the correction discussed in the *SI Text*, corresponds to a minimal true stiffness $\kappa^{\mathrm{twist}}(\mathrm{stator}) > 500$ pNnm.

The situation was different if $\mathbf{b_2}$ was bent rather than twisted. The red data in Fig. 5 were obtained for the bead attachment as in Fig. 1*C*. Here, the apparent fluctuation widths (FWHM) of the three forms, 4° (1wt*), 9.7° (long), and 15° (3-gly), significantly differed from each other. The apparent stiffness was $\kappa^{\mathrm{bent}}_{\mathrm{app}}(\mathrm{stator}) = 4{,}600$ pNnmrad^{-2} (wt*), 780 (long), and 330 (3-gly), respectively. Upon correction (see above), the true stiffness amounts to at least $\kappa^{\mathrm{bent}}(\mathrm{stator}) = 700$, 350, and 200 pNnm, respectively. The apparent stiffness that has been previously reported for the elastically most compliant domain on the rotor of $\mathrm{EF_0EF_1}$, namely, $\kappa_{\mathrm{app}}(\mathrm{rotor}) = 70$ pNnm (13), and after correction (see *SI Text*) $\kappa(\mathrm{rotor}) \geq 20$ pNnm, is much smaller than

		1 … 65 … 66 … 73
*wt**	*SD306*	M**C**LNATILGQAIAFVLFVLFCMKYVWPPLMAAIEKRQKEIADGLASAERAHKDLDLAKASATDQL----------KKAKAEAQ
	GH33	MNLNATILGQAIAFVLFVLFCMKYVWPPLMAAIEKRQKEIADGLASAERAHKDLDLAKASATDQL----------KKAKAEAQ
3-gly	*SD390*	M**C**LNATILGQAIAFVLFVLFCMKYVWPPLMAAIEKRQKEIADGLASAERAHKDLDLAKASATDQL----------KKAKAEAQ
	SD466	MNLNATILGQAIAFVLFVLFCMKYVWPPLMAAIEKRQKEIADGLASAERAHKDLDLAKASATDQL----------KKAKAEAQ
long	*BDC307*	M**C**LNATILGQAIAFVLFVLFCMKYVWPPLMAAIEKRQKEIADGLASAERAHKDLDLAKASATDQL**DLAKASATDQL**KKAKAEAQ
	SD460	MNLNATILGQAIAFVLFVLFCMKYVWPPLMAAIEKRQKEIADGLASAERAHKDLDLAKASATDQL**DLAKASATDQL**KKAKAEAQ
		<-transmembrane domain-><- tether domain -><- dimerization domain

		74 … 156
*wt**	*SD306*	VIIEQANKRRSQILDEAKAEAEQERTKIVAQAQAEIEAERKRAREELRKQVAILAVAGAEKIIERSVDEAANSDIVDKLVAEL
	GH33	VIIEQANKRRSQILDEAKAEAEQERTKIVAQAQAEIEAERKRAREELRKQVAILAVAGAEKIIERSVDEAANSDIVDKLVAEL
3-gly	*SD390*	VIIEQAN**GGG**SQILDEAKAEAEQERTKIVAQAQAEIEAERKRAREELRKQVAILAVAGAEKIIERSVDEAANSDIVDKLVAEL
	SD466	VIIEQAN**GGG**SQILDEAKAEAEQERTKIVAQAQAEIEAERKRAREELRKQVAILAVAGAEKIIERSVDEAANSDIVDKLVAEL
long	*BDC307*	VIIEQANKRRSQILDEAKAEAEQERTKIVAQAQAEIEAERKRAREELRKQVAILAVAGAEKIIERSVDEAANSDIVDKLVAEL
	SD460	VIIEQANKRRSQILDEAKAEAEQERTKIVAQAQAEIEAERKRAREELRKQVAILAVAGAEKIIERSVDEAANSDIVDKLVAEL
		dimerization domain -><- delta-binding domain ->

Fig. 4. Amino acid sequences of the **b** subunits of analyzed strains. Sequence modifications are highlighted in bold letters. Trivial names (*Left*) are self-evident.

the former figure for the stator, which holds true in the wt* and both mutants.

Effects of Stator Mutations on Energy Coupling by ATP Synthase. Oxidative phosphorylation in vivo was assessed by the ability of the **b**N2C-type plasmids to support growth of the *unc* deletion strain DK8 on minimal media containing 0.2% succinate as carbon and energy source. As an additional control to ensure that the side chains eliminated by the 3-gly mutation did not have important specific interactions with $\alpha_3\beta_3$, a mutant with positions 80–83 substituted by alanine ("4-ala") was included in these studies. Succinate-dependent growth equivalent to the KH4 WT was supported by the bN2C and the 4-ala mutant. In contrast, the long mutant grew only very slightly, as in previous work (14), and the 3-gly mutant exhibited no growth on succinate. Membrane preparations from strains grown on rich media revealed that the levels of assembled ATPase were also affected, the largest change being due to the bN2C mutation itself. Mutations in the coiled-coil region resulted in some further effects on assembly, but the differences in ATPase levels between the 4-ala mutant and the others were fairly modest compared to the growth impairment.

The ATP-dependent H^+ pumping activity of the same membrane preparations was tested by the 9-amino-6-chloro-2-methoxyacridine (ACMA) fluorescence quenching method. To correct for the different levels of ATPase in the membrane samples, the amounts added to the assays were normalized to the same total membrane-bound ATPase activity. Fig. 6 documents the proton pumping activity of the wild-type and mutant enzymes. Membranes from all of the strains that supported full growth on succinate gave similar levels of fluorescence quenching, validating the approach. In comparison, membranes from the long and 3-gly mutants were also active, though less so.

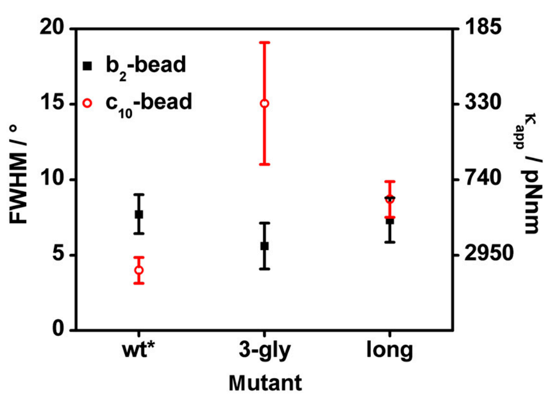

Fig. 5. The FWHM of thermal rotary fluctuations of the stator of EF_OF_1 in the wild type and **b** mutants analyzed for either way of deformation according to Fig. 1 *B* (black, bead attachment to $\mathbf{b_2}$) and *C* (red, bead attachment to $\mathbf{c_{10}}$ and cross-link between **a** and **c**). The left scale shows the FWHM of thermal fluctuations in degrees, and the right scale the apparent torsional stiffness corresponding to the mean FWHM (see Eq. **2**). The error bars refer to cumulated data from between 4 (3-gly, black) and 13 (wt*, black) over 8 (the rest) single molecules, each.

Discussion

The two stepping motors of the F_OF_1-ATPase are coupled by an elastic power transmission. Whereas the stator is very stiff, as demonstrated in the present work, the major elastic buffers are located on the central rotor and on the lever of subunit β, right between the two sites of torque generation in F_O and F_1 (13). Because of the limited video time resolution, the previously assigned stiffness of the rotor, 70 pNnm (13), must be corrected to yield smaller values, say 20 pNnm or greater (see *SI Text* and Fig. S5). Still, in the wt* enzyme, the stator was at least 10 times stiffer (700 pNnm) than the most compliant domain on the rotor. The $\mathbf{b_2}$ homodimer forms a rather stiff scaffold to hold the elec-

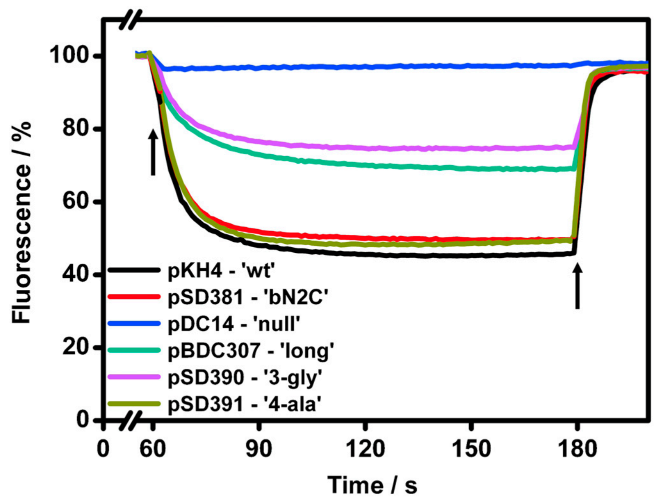

Fig. 6. The effect of long and 3-gly mutations on ATP-dependent H^+ pumping. ATP-dependent quenching of ACMA fluorescence was carried out to measure H^+ pumping. Each 2-mL assay received an amount of membranes containing 0.1 unit of membrane-bound ATPase activity. The negative control membranes, from cells carrying the ATP synthase null plasmid pDC42, received 0.6 mg of membrane protein, slightly greater than the ATPase-positive strain with the lowest activity, 3-gly. Arrows at 60 and 180 s indicate the additions of 0.15 mM ATP and 0.2 μM nigericin as protonophore.

tromotor, F_O, and the chemical generator, F_1, firmly together. The **b** subunit is 156-residues long. The N-terminal segment is tightly associated with $\mathbf{ac_{10}}$ of EF_O, and the C-terminal portion with αβδ of EF_1. The region in between, positions 55–110 where the right-handed coiled-coil motif is evident, seems to lack specific tight contacts with the rest of the enzyme, because it can be replaced by the corresponding sequences from other bacterial **b** subunits without loss of assembly or function (24). We anticipate that this segment is the only one prone to deformation by the opposing motors.

Two groups have evaluated the *lateral stiffness* (κ^{lat}) of the α-helical coiled coil of myosin II (25, 26) (for the composite cross-bridge stiffness of holomyosin see ref. 27). How does the rotary stiffness of the stator of F_OF_1 correlate with the lateral stiffness of these α-helical coiled coils? The lateral stiffness of the stator can be inferred from its rotary stiffness by the following consideration. When the electromotor generates torque and ATP-hydrolysis countertorque such that the $\mathbf{c_{10}}$ ring (attached to $\mathbf{ab_2}$) rotates by an angle ΔΘ (see Fig. 1*C*), $\mathbf{b_2}$ is bent, and its N-terminal end is displaced by Δy which relates to the rotary displacement, ΔΘ, and the radius (r) as follows:

$$\Delta y = r \cdot \Delta\Theta. \qquad [3]$$

Application of this equation to the observed rotary fluctuations allows one to calculate the following lateral stiffnesses: $\kappa^{lat}_{wt} \cong 77$ pNnm^{-1}, $\kappa^{lat}_{long} \cong 49$ pNnm^{-1}, and $\kappa^{lat}_{3\text{-}gly} \cong 22$ pNnm^{-1}.

Let us compare this lateral stiffness of the whole stator to the reported stiffness of coiled coils of myosin II (25, 26). (*i*) Rief and coworkers (25) arrived at a persistence length of the coiled coil of myosin of 25 nm. The persistence length (L_p) of a semiflexible filament is related to the lateral stiffness of the respective cantilever as follows (28):

$$\kappa^{lat} = \frac{3L_p \cdot k_B T}{L^3}, \qquad [4]$$

where k_B denotes the Boltzmann constant, T the temperature in Kelvin, and L the length of the cantilever. When assuming the same persistence length as in myosin II for $\mathbf{b_2}$ and assuming a free length of 5 nm, one arrives at a stiffness of $\kappa^{lat}_{5\ nm} \cong 2.7$ pNnm^{-1}. In other words, a segment of 5-nm length of the coiled coil of myosin II is more compliant than the stator of EF_OF_1. (*ii*) The bending of the coiled coil of the myosin II S2 subdomain has been theoretically studied by Karplus and coworkers (26) using nonequilibrium molecular dynamics and normal mode analysis. They predicted a lateral stiffness of $\kappa^{lat}_{S2} \cong 0.01$ pNnm^{-1} for the 60-nm long S2 domain. When scaling this figure down to a shorter length (5 nm), one arrives at an estimated $\kappa^{lat}_{5\ nm} \cong 17$ pNnm^{-1}, i.e., the same order of magnitude as inferred for 5 nm of the $\mathbf{b_2}$ homodimer.

These results reveal that the coiled coil of the **b** heterodimer functions as a comparatively rigid stator stalk, by itself and by its interaction with the other subunits of F_O on the one side and of F_1 on the other. The above data on the relative proton pumping activities of the membrane-bound enzyme (100% for wt* and about 50% for both mutants, long and 3-gly) indicate that lowering of the stator stiffness is without dramatic effect on the coupling efficiency, probably because the stator was by at least one order of magnitude stiffer than the rotor in all cases. It has remained to be established by structural studies how exactly the additional length (three helix turns) of the long mutant is accommodated by the enzyme.

The well-known tendency of glycine to reduce helix stability led us to construct the 3-gly mutant as an approach to reduce the stability of the helices without disrupting the normal interactions of the N- and C-terminal regions of **b** with the rest of the enzyme, or to affect the structure in the resting state. Because both chimeric **b** subunits incorporating **b** sequences from other eubacteria and the 4-ala mutation described here had wild-type properties, it is unlikely that loss of specific interactions with $\alpha_3\beta_3$ were responsible for the major effect on stiffness. We again suspect that the offset nature of the helices played a role, as one or the other of the helices is affected over most of a region more than 1 nm in length (see Fig. S4).

The directionality of the strain on $\mathbf{b_2}$ is the same, independent of whether ATP hydrolysis (by F_1) or protonmotive force (by F_O) provides the dominant driving torque. It is tempting to speculate that it tightens the coiled coil. For two reasons, there is not yet a ready answer. (*i*) The pitch in the only available crystal structure is much larger (45 nm, see ref. 23) than the small "free" portion of $\mathbf{b_2}$ (5 nm), and (*ii*) the binding strength of the two copies of **b** to F_1 cannot be predicted. This question has to be left for future studies.

Summary

Coiled coils occur in many different proteins where they act as spacers or elastic connectors between protein domains. This experimental study assessed the twisting and bending stiffness of a molecular device which is stabilized by an extended α-helical coiled coil. In the F_OF_1-ATPase from *E. coli*, a homodimer of the **b** subunit forms a right-handed α-helical coiled coil that stretches out from its membrane anchor—in contact with subunit **a** and the $\mathbf{c_{10}}$ ring of EF_O—up to the top of EF_1 where it contacts subunits α, β, and δ, the latter with nanomolar binding affinity (see ref. 4 and references therein). In this work, we found that the stator of the *E. coli* enzyme, with $\mathbf{b_2}$ as its most extended component, was much stiffer than the rotor. This also holds in the WT and in both mutants tested, namely, with **b** extended by 11 residues and with its α-helical structure destabilized by substitution of three glycines in a row. We conclude that the stiff stator acts as the scaffold for the two rotary motors, F_O and F_1, and the at least 10-fold more compliant rotor as the elastic power transmission between them. Although the dynamics of nanomachinery because of its stochastic nature fundamentally differs from the one of macroscopic devices, elastic power transmission is a common principle for coupling steppers (as in F-ATPase and, e.g., a rolling mill).

Materials and Methods

Molecular Genetics. This work was conducted using forms of ATP synthase carried on two types of plasmids, pGH33 and pSD306, and their derivatives. Both types of plasmids were derived from pKH4 (29) and had all wild-type cysteines substituted by alanines and a his tag at the N terminus of the β-subunit. Plasmid pGH33 (13) also carried a strep-tag at the C terminus of subunit **c** and a pair of introduced cysteine residues in subunits **a** (**a**I223C) and **c** (**c**L72C). Plasmid pSD306 was identical to pKH4 except that it carried a cysteine mutation near the N terminus of subunit **b**, namely, **b**N2C. Plasmid pSD381 ($\mathbf{b_{syn}}$) encoded the same polypeptide sequences as pSD306 but incorporated a portion of the synthetic *uncF* gene (30) to facilitate cloning of mutations. Plasmid pSD390 (3-gly) was identical to pSD381 except that mutations encoded glycine residues at three consecutive **b** sequence positions, Lys^{81}-Arg^{83}. Plasmid pSD391 was identical to pSD381 except that mutations encoded alanine residues at four consecutive **b** sequence positions, Asn^{80}–Arg^{83}. Plasmid pBDC307 (long) was identical to pSD306 except that positions Asp^{55}–Leu^{65} of the **b** sequence were repeated in tandem, as in the previously described pAUL47 (14). Derivatives of plasmid pGH33 containing the 3-gly (pSD466) and long (pSD460) mutations in the coiled-coil domain of **b** were also constructed. New mutations in the **b** subunit sequence were generated by PCR mutagenesis and introduced into cloning plasmids containing fragments of the unc operon subcloned from pKH4. Both these and previously described mutations were moved into the larger plasmids by ligation of appropriate restriction endonuclease fragments.

Expression and Purification of EF_OF_1. Transformed strains were grown in minimal medium (31). Membranes were purified as described previously (13). Membrane extraction was carried out essentially as described (32). Glycerol was added to eluates to a final concentration of 50% (vol/vol) before they were stored at −80 °C before use.

Preparation of Magnetic Beads. Steptactin- (IBA-Göttingen) or Streptavidin-coated hyperparamagnetic beads (Roche) (typical diameter 1 μm) were prepared as described (13).

Oxidation of EF_OF_1. To close the disulfide bridge, the enzyme was diluted with the same volume of a buffer containing 50 mM MOPS/KOH (pH 7.5), 50 mM KCl, 5 mM $MgCl_2$, 0.5% (wt/vol) *N*-octyl-L-D-glucopyranoside, and 10% (vol/vol) glycerol, respectively (buffer MD), and added with 5,5′-dithio-bis(2-nitrobenzoate acid) final concentration of 1 mM. Before observation started, the enzyme was incubated for at least for 30 min.

Immobilization of EF_OF_1. Samples were filled into flow cells consisting of two coverslips (bottom, 26×76 mm^2; top, 24×24 mm^2) separated by double-adhesive tape (Tesa-Beiersdorf). EF_OF_1 protein solutions were stepwise infused in the following order (50 μL per step, 4 min incubation): (*i*) 0.8 μM Ni-NTA-HRP conjugate in buffer MD; (*ii*) wash with buffer MD; (*iii*) 10 mg/mL BSA in buffer MD; (*iv*) wash with buffer MD; (*v*) 1 μM EF_OF_1 in buffer MD; (*vi*) wash with buffer MD; (*vii*) 20-fold diluted prepared magnetic beads in buffer MD; (*viii*) wash with buffer MD; (*ix*) 500.000-fold diluted Q dots in buffer MD; (*x*) wash with buffer MD; (*xi*) 20 mM glucose, 0.2 mg/mL glucose oxidase, 50 μg/mL catalase, and 5 mM ATP in buffer MD, respectively.

Video Microscopy. EF_OF_1 constructs were observed, and single molecule movement was recorded with an inverted fluorescence microscope as published elsewhere (19). Video data were captured with a TerraTec Grabster AV 250 video card, digitized directly, and edited with VirtualDub 1.98. A software program for evaluation of the obtained video sequences was written with Matlab 6.5.

Minimal Media Growth Tests and Characterization of Membrane Activities. Determination of ability to support growth on M9 minimal media supplemented with either 0.2% succinate or 0.2% glucose as carbon and energy source, preparation of membrane vesicles from cells grown on rich media, and determination of membrane-bound ATPase activity were carried out as described (24, 33). ATP-dependent proton pumping was measured by the quenching of fluorescence of 1 μM ACMA following addition of 0.15 mM ATP, using the method of D'Alessandro et al. (34). After the quenching phase, 0.2 μM nigericin was added to dissipate the proton gradient.

ACKNOWLEDGMENTS. The authors thank Hella Kenneweg and Gabriele Hikade for excellent technical assistance, and Dr. Richard Berry, Oxford, for valuable advice. The Volkswagen Foundation provided financial support to W.J., the European Union to W.J. and S.E., the Niedersächsische Ministerium für Wissenschaft und Kultur to W.J., the Canadian Institutes of Health Research (FRN10237) to S.D.D., and the US Public Health Service (GM70978) to B.D.C.

1. Junge W, Sielaff H, Engelbrecht S (2009) Torque generation and elastic power transmission in the rotary F_OF_1-ATPase. *Nature* 459:364–370.
2. von Ballmoos C, Cook GM, Dimroth P (2008) Unique rotary ATP synthase and its biological diversity. *Annu Rev Biophys* 37:43–64.
3. Revington M, McLachlin DT, Shaw GS, Dunn SD (1999) The dimerization domain of the b subunit of the *Escherichia coli* F(1)F(0)-ATPase. *J Biol Chem* 274:31094–31101.
4. Claggett SB, O'Neil Plancher M, Dunn SD, Cain BD (2009) The b subunits in the peripheral stalk of F1F0 ATP synthase preferentially adopt an offset relationship. *J Biol Chem* 284:16531–16540.
5. Del Rizzo PA, Bi Y, Dunn SD (2006) ATP synthase b subunit dimerization domain: A right-handed coiled coil with offset helices. *J Mol Biol* 364:735–746.
6. Abrahams JP, Leslie AGW, Lutter R, Walker JE (1994) The structure of F1-ATPase from bovine heart mitochondria determined at 2.8 Å resolution. *Nature* 370:621–628.
7. Pogoryelov D, Yildiz O, Faraldo-Gomez JD, Meier T (2009) High-resolution structure of the rotor ring of a proton-dependent ATP synthase. *Nat Struct Mol Biol* 16:1068–1073.
8. Cherepanov DA, Mulkidjanian A, Junge W (1999) Transient accumulation of elastic energy in proton translocating ATP synthase. *FEBS Lett* 449:1–6.
9. Pänke O, Rumberg B (1999) Kinetic modeling of rotary CF_0F_1-ATP synthase: Storage of elastic energy during energy transduction. *Biochim Biophys Acta* 1412:118–128.
10. Junge W, et al. (2001) Inter-subunit rotation and elastic power transmission in F_oF_1-ATPase. *FEBS Lett* 504:152–160.
11. Pänke O, Cherepanov DA, Gumbiowski K, Engelbrecht S, Junge W (2001) Viscoelastic dynamics of actin filaments coupled to rotary F-ATPase: Torque profile of the enzyme. *Biophys J* 81:1220–1233.
12. Elston T, Wang H, Oster G (1998) Energy transduction in ATP synthase. *Nature* 391:510–514.
13. Sielaff H, et al. (2008) Domain compliance and elastic power transmission in rotary FOF1-ATPase. *Proc Natl Acad Sci USA* 105:17760–17765.
14. Sorgen PL, Bubb MR, Cain BD (1999) Lengthening the second stalk of F_1F_0 ATP synthase in *Escherichia coli*. *J Biol Chem* 274:36261–36266.
15. Sorgen PL, Caviston TL, Perry RC, Cain BD (1998) Deletions in the second stalk of F1F0-ATP synthase in *Escherichia coli*. *J Biol Chem* 273:27873–27878.
16. Rees DM, Leslie AG, Walker JE (2009) The structure of the membrane extrinsic region of bovine ATP synthase. *Proc Natl Acad Sci USA* 106:21597–21601.
17. Carbajo RJ, et al. (2007) How the N-terminal domain of the OSCP subunit of bovine F1Fo-ATP synthase interacts with the N-terminal region of an alpha subunit. *J Mol Biol* 368:310–318.
18. Dickson VK, Silvester JA, Fearnley IM, Leslie AG, Walker JE (2006) On the structure of the stator of the mitochondrial ATP synthase. *EMBO J* 25:2911–2918.
19. Pänke O, Gumbiowski K, Junge W, Engelbrecht S (2000) F-ATPase: Specific observation of the rotating c subunit oligomer of EF_OEF_1. *FEBS Lett* 472:34–38.
20. Berry RM, Berg HC (1996) Torque generated by the bacterial flagellar motor close to stall. *Biophys J* 71:3501–3510.
21. Okuno D, Iino R, Noji H (2010) Stiffness of gamma subunit of F_1-ATPase. *Eur Biophys J* 39:1589–1596.
22. Howard J (2001) *Mechanics of Motor Proteins and Cytoskeleton* (Sinauer, Sunderland, MA), Chap 4.
23. Lee LK, Stewart AG, Donohoe M, Bernal RA, Stock D (2010) The structure of the peripheral stalk of *Thermus thermophilus* H^+-ATPase/synthase. *Nat Struct Mol Biol* 17:373–378.
24. Bi Y, Watts JC, Bamford PK, Briere LK, Dunn SD (2008) Probing the functional tolerance of the b subunit of *Escherichia coli* ATP synthase for sequence manipulation through a chimera approach. *Biochim Biophys Acta* 1777:583–591.
25. Schwaiger I, Sattler C, Hostetter DR, Rief M (2002) The myosin coiled-coil is a truly elastic protein structure. *Nat Mater* 1:232–235.
26. Adamovic I, Mijailovich SM, Karplus M (2008) The elastic properties of the structurally characterized myosin II S2 subdomain: A molecular dynamics and normal mode analysis. *Biophys J* 94:3779–3789.
27. Veigel C, Bartoo ML, White DC, Sparrow JC, Molloy JE (1998) The stiffness of rabbit skeletal actomyosin cross-bridges determined with an optical tweezers transducer. *Biophys J* 75:1424–1438.
28. Sackmann E, Merkel R (2010) *Lehrbuch der Biophysik* (Wiley, Weinheim, Germany), Chap 24.
29. Noji H, et al. (1999) Rotation of *Escherichia coli* F(1)-ATPase. *Biochem Biophys Res Commun* 260:597–599.
30. McLachlin DT, Dunn SD (1997) Dimerization interactions of the b subunit of the *Escherichia coli* F_1F_0-ATPase. *J Biol Chem* 272:21233–21239.
31. Langemeyer L, Engelbrecht S (2007) Essential arginine in subunit a and aspartate in subunit c of F(o)F(1) ATP synthase. Effect of repositioning within Helix 4 of subunit a and Helix 2 of subunit c. *Biochim Biophys Acta* 1767:998–1005.
32. Ishmukhametov RR, Galkin MA, Vik SB (2005) Ultrafast purification and reconstitution of His-tagged cysteine-less *Escherichia coli* F1Fo ATP synthase. *Biochim Biophys Acta* 1706:110–116.
33. Cipriano DJ, Bi Y, Dunn SD (2002) Genetic fusions of globular proteins to the epsilon subunit of the *Escherichia coli* ATP synthase: Implications for in vivo rotational catalysis and epsilon subunit function. *J Biol Chem* 277:16782–16790.
34. D'Alessandro M, Turina P, Melandri BA (2008) Intrinsic uncoupling in the ATP synthase of *Escherichia coli*. *Biochim Biophys Acta* 1777:1518–1527.

Suporting Information

Wächter et al. 10.1073/pnas.1011581108

SI Text

True and Apparent Stiffness, Correction for Limited Video Frequency. ***Magnetic beads (typical radius 0.5 μm).*** Thermal fluctuations, if recorded by video at a given frame rate, are averaged over the frame duration, such that their apparent variance is less than the true one. In the context of this work, this variance leads to overestimation of the elastic stiffness of a given bead-spring construct. The following error discussion is based on chapter 4 ("Thermal Forces and Diffusion") in ref. 1.

Rotary motion of a microscaled bead attached to a torsion spring is overdamped and its autocorrelation function decays exponentially:

$$R(t) = \frac{k_B T}{\kappa} \exp(-\frac{\kappa}{\gamma} t). \quad \text{[S1]}$$

Herein k_B denotes the Boltzmann constant, T the temperature, κ the elastic stiffness of the torsion spring, γ the viscous drag coefficient of the bead, and t the time.

The magnitude of R at time zero equals the variance, σ^2, which is a consequence of the equipartition principle:

$$R(0) = \frac{k_B T}{\kappa} = \sigma^2 \quad \text{[S2]}$$

The so called "power spectrum" of the autocorrelation function, $G(\omega)$, its Fourier transform, reads as follows:

$$G(\omega) = 4 \int_0^\infty R(t) \cdot \cos \omega t \cdot dt = \frac{4 k_B T \gamma}{\kappa^2} \cdot \frac{1}{[1 + (\frac{\omega}{\omega_0})^2]}, \quad \text{[S3]}$$

where ω denotes the angular frequency and ω_0 the "corner frequency" (or cutoff frequency) of the Lorentzian spectrum,

$$\omega_0 = \frac{\kappa}{\gamma}. \quad \text{[S4]}$$

When presented as the reverse Fourier transformation, $R(t)$ reads

$$R(t) = \frac{1}{2\pi} \int_0^\infty G(\omega) \cdot \cos \omega t \cdot d\omega \quad \text{[S5]}$$

and at time zero

$$R(0) = \frac{1}{2\pi} \int_0^\infty G(\omega) \cdot d\omega = \frac{2}{\pi} \cdot \frac{k_B T}{\kappa} (\arctan \frac{\infty}{\omega_0}) = \frac{k_B T}{\kappa}, \quad \text{[S6]}$$

see Eq. **S2** above.

If the fluctuations are recorded by an instrument with limited time resolution, as in video recordings, fluctuations occurring at higher frequencies than the limiting frequency of the instrument are suppressed. As a consequence, the apparent variance is smaller and the apparent stiffness greater than the respective true one:

$$R_{app}(0) = \frac{1}{2\pi} \int_0^{\omega_l} G(\omega) \cdot d\omega = \frac{2}{\pi} \cdot \frac{k_B T}{\kappa} \cdot \arctan \frac{\omega_l}{\omega_0} = \sigma^2_{app} = \frac{k_B T}{\kappa_{app}}. \quad \text{[S7]}$$

The true stiffness (κ) is smaller than the apparent stiffness (κ_{app}), and the correction factor depends on the ratio between the limiting frequency (ω_l) and the corner frequency (ω_0) of the Lorentzian (Eq. **S4**):

$$\kappa = \frac{\arctan \omega_l / \omega_0}{\pi/2} \cdot \kappa_{app}. \quad \text{[S8]}$$

According to the sampling theorem, the limiting frequency of a digital recording is half the sampling frequency. In the present video system, the frame rate was 25 s^{-1}. The limiting angular frequency then is

$$\omega_l = 1/2 \cdot 2\pi \cdot 25 \ s^{-1}. \quad \text{[S9]}$$

The angular corner frequency (ω_0, see Eq. **S4**) is difficult to assess with precision. The attachment mode of the bead to the spring (central versus off-central), variations of the bead diameter, and flow coupling between bead and surface all affect the viscous drag coefficient, γ. A centrally rotating bead ($\gamma = 8\pi\eta R^3$) moving in bulk water ($\eta_{H_2O} = 10^{-3}$ kgm^{-1} s^{-1}) gives the lowest estimate for the drag coefficient and thus an upper limit for the corner frequency. For a bead radius of 0.5 μm,

$$\omega_0 \leq \omega_0^{(a)} = \frac{\kappa}{3.14}, \quad \text{[S10]}$$

where κ comes in piconewton nanometer.

The relation between the apparent and the true stiffness is plotted in Fig. S5 for two different viscous drag coeeficients, the one of a centrally attached sphere (radius 0.5 μm) moving in bulk water, and a threefold larger drag (accounting for eccentric attachment and higher viscosity due to flow coupling).

It is obvious from Fig. S5 that video-recorded fluctuations of a bead with 0.5-μm radius yielding an apparent stiffness of up to 200 pNnm approximate the true stiffness reasonably well. An apparent stiffness of 500 pNnm may be up to twofold overrated, and the overrating increases further with growing κ_{app}.

In the context of the present work, two properties are noteworthy: (*i*) The order of apparent stiffness monotonously follows the order of true stiffness; in other words, differences are meaningful, whether corrected or not. (*ii*) An apparent stator stiffness of 1,700 pNnm implies a true stiffness of at least 500 pNnm, which is still at least 10 times more rigid than the most flexible domain on the rotor of EF_OF_1 whose corrected stiffness is 35 pNnm (see below). In other words, the conclusions of Sielaff et al. (2) and this work are valid and independent of the correction, namely, (*i*) F_O and F_1 are linked by a stiff stator, and (*ii*) their cooperation is smoothed by an elastically compliant rotor.

Actin filaments (typical length 0.5–0.8 nm). In previous experiments aiming mainly at the stiffness of the rotor in EF_0F_1, we used actin filaments as probes and selected those single filaments that were fixed at one end to the enzyme and discarded those fixed in the middle and rotating as a propeller (2). The respective drag coefficient is

$$\gamma_{fil} = \frac{4\pi\eta L^3}{3(\ln L/r - 0.447)}, \quad \text{[S11]}$$

where η is the medium viscosity, L the length, and r the cylinder radius of the filament.

Assuming a length of 0.8 μm, a radius of 2.8 nm, the viscosity as in pure water 10^{-3} kgm^{-1} s^{-1}, and a true stiffness of 35 pNnm, the calculated corner frequency of the respective Lorentzian is $\omega_0 = 83$ s^{-1}, such that the apparent stiffness is 75 pNnm as reported for EF_OF_1 with the filament attached to the c ring (bending mode of deformation) and the engineered disulfide lock between rotor and stator placed in the top of EF_1 (2). The elastically highly compliant domain between F_O and F_1 is thus probably twofold more flexible than was previously reported.

1. Howard J (2001) *Mechanics of Motor Proteins and Cytoskeleton* (Sinauer, Sunderland, MA).

2. Sielaff H, et al. (2008) Domain compliance and elastic power transmission in rotary F_OF_1-ATPase. *Proc Natl Acad Sci USA* 105:17760–17765.

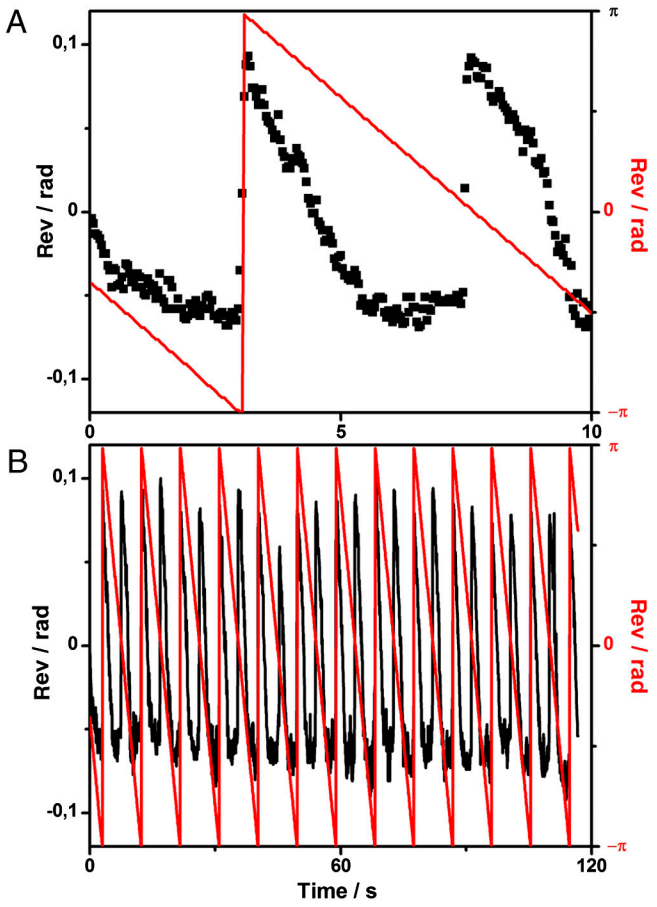

Fig. S1. Magnetorotation trajectory of the same bead-EF_OF_1 constructs as shown in Movie S1 [black; mutant SD466 (3-gly)]. Two magnets were mounted at opposite positions on a rotating disk. The rotation rate was 0.107 rev/s. The rotary trajectory of the disk between $-\pi$ and $+\pi$ is shown in red, the trajectory of the bead in black. The relaxed orientation of the bead in absence of a magnetic field is set at 0°. (*A*) Excerpt of first 10 s, and (*B*) full trajectory over 2 min. Every single frame-based bead position is shown as a quad.

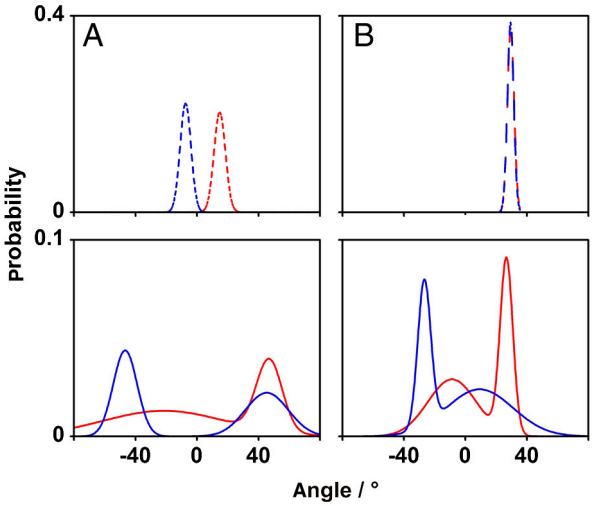

Fig. S2. Histograms of thermal fluctuations (*Upper*) and magnetically forced rotation of two single bead-EF_OF_1 constructs that did not fulfill the symmetry requirements detailed in the text. Both datasets were obtained on mutant SD460 ("long").

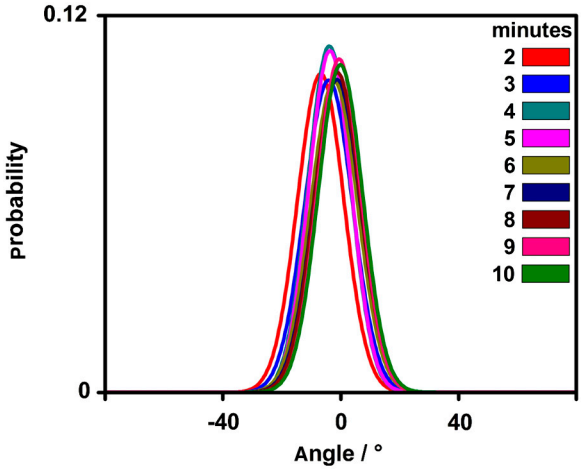

Fig. S3. Thermal rotational fluctuations recorded with one single bead-EF_OF_1 construct which was sampled and averaged over intervals of up to a duration of 10 min.

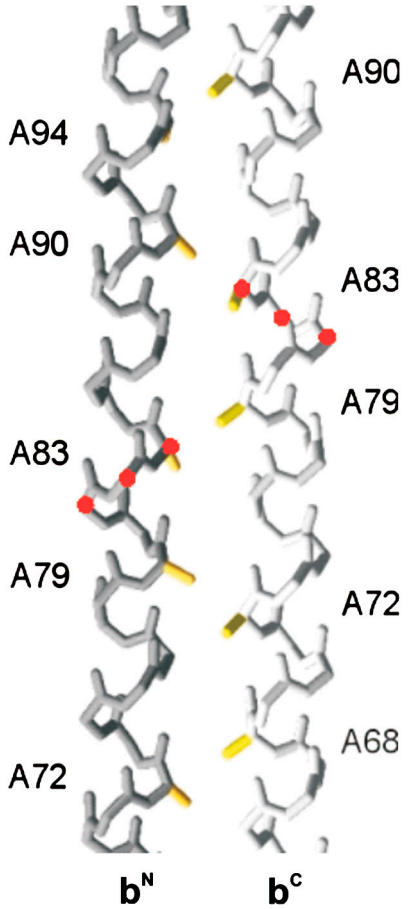

Fig. S4. Model structure of the right-handed coiled coil of $\mathbf{b_2}$ that is slightly off-register. The red dots indicate the C_α atoms with glycine substitution in the mutant 3-gly.

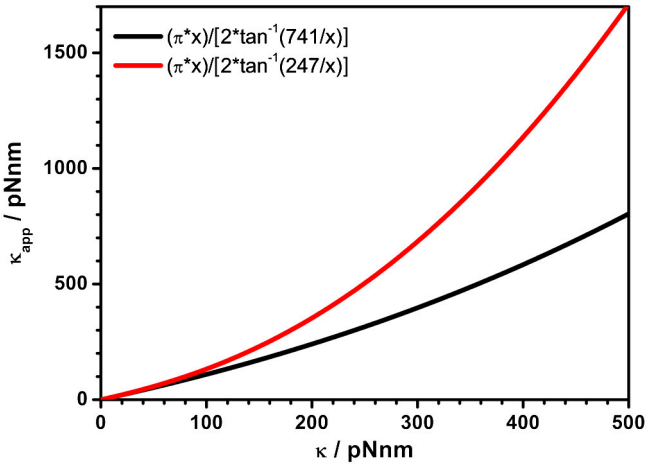

Fig. S5. Apparent versus true stiffness calculated according to Eq. **S8** (see text).

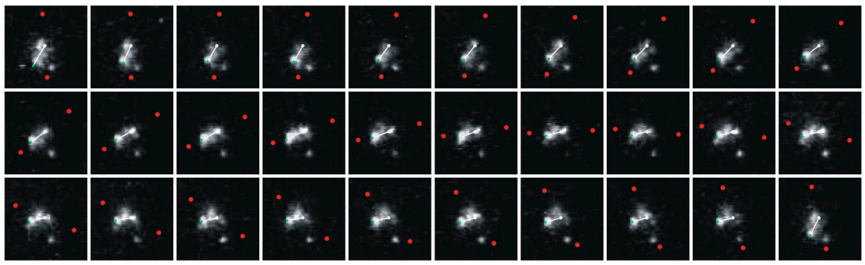

Movie S1. Forced rotation of magnetic bead attached to the stator of EF_OF_1.

Movie S1 (MOV)